Myosin Va and myosin VI coordinate their steps while engaged in an in vitro tug of war during cargo transport

M. Yusuf Ali[a], Guy G. Kennedy[a], Daniel Safer[b], Kathleen M. Trybus[a], H. Lee Sweeney[b,c], and David M. Warshaw[a,1]

[a]Department of Molecular Physiology and Biophysics, University of Vermont, Burlington, VT 05405; [b]Department of Physiology and [c]Pennsylvania Muscle Institute, University of Pennsylvania School of Medicine, 3700 Hamilton Walk, Philadelphia, PA 19104-6085

Edited* by Thomas D. Pollard, Yale University, New Haven, CT, and approved July 13, 2011 (received for review March 17, 2011)

Myosin Va (myoV) and myosin VI (myoVI) are processive molecular motors that transport cargo in opposite directions on actin tracks. Because these motors may bind to the same cargo in vivo, we developed an in vitro "tug of war" to characterize the stepping dynamics of single quantum-dot-labeled myoV and myoVI motors linked to a common cargo. MyoV dominates its myoVI partner 79% of the time. Regardless of which motor wins, its stepping rate slows due to the resistive load of the losing motor (myoV, 2.1 pN; myoVI, 1.4 pN). Interestingly, the losing motor steps backward in synchrony with the winning motor. With ADP present, myoVI acts as an anchor to prevent myoV from stepping forward. This model system emphasizes the physical communication between opposing motors bound to a common cargo and highlights the potential for modulating this interaction by changes in the cell's ionic milieu.

intracellular transport | motility assay | processivity | single molecule biophysics

Intracellular cargo transport relies on at least two classes of myosin molecular motors to navigate the actin cytoskeleton. Class V (myoV) and class VI (myoVI) myosins are double-headed motors that transport cargo in opposite directions along polarized actin filament tracks (1, 2). These motors convert the energy of ATP hydrolysis into force and motion and in doing so step processively on actin in a hand-over-hand fashion. With the plus-ends of actin filaments oriented toward the cell periphery, myoV transport contributes to exocytosis, whereas myoVI transport is critical to endocytosis (1, 2). Ensembles of molecular motors share the responsibility for transporting a single vesicle. For example, approximately 60 myoV motors coat a melanosome, although a smaller number is likely to be engaged with the track at any given time (3). Transport can also be bidirectional when oppositely directed motors are operative, as for axonal transport by the microtubule-based motors, kinesin and dynein (4, 5). With myoV and myoVI colocalizing to organelles (6, 7), these motors may engage in a virtual tug of war. If so, how do these oppositely directed myosin motors mechanically interact so that cargo is efficiently delivered to its destination?

Individual motors within a transport ensemble may coordinate, cooperate, or mechanically impede one another, but determining by which mode they operate is complicated by the cargo geometry, the number and directionality of engaged motors, and the physical challenges presented by the dense actin cytoskeleton. Therefore, investigators have designed in vitro experiments to limit the number of coupled motors so that mechanistic modeling efforts were tractable (8–11). For these models, the velocity and direction of cargo transport generated by ensembles of antagonistic motors depended solely on the relative number of motors pulling in either direction (12, 13). The mechanical interactions between motors and the resultant stepping dynamics of each motor within the ensemble were beyond the predictive capacity of these models. Therefore, we developed an in vitro model system in which a single myoV molecule was physically linked to an oppositely directed single myoVI through a common cargo in order to characterize the mechanical interactions during this virtual tug of war. Using different color fluorescent quantum dots (Qdots) to label each motor, we unambiguously determined each motor's stepping dynamics with nanometer resolution. This model system is more biologically relevant because the mechanical interactions and resistive loads occur between the cargo-bound motors rather than being applied through, for example, an optical trap (14–18). Here, we report that myoV is the dominant motor and that, as myoVI resists, it steps backward in coordination with myoV's forward steps. Although myoV dominating suggests that intracellular cargo transport would be unidirectional when equal numbers of both motors are present, myoVI can prevent myoV from dominating by myoVI shifting its role from transporter to anchor in the presence of ADP, thus, potentially linking cargo transport to the cell's metabolic state (19).

Results

MyoV and MyoVI Coupled Motor Complex. The stepping dynamics of coupled myoV and myoVI motors were observed by labeling one myoV head with a green Qdot ($\lambda = 565$ nm) and by labeling the exchangeable calmodulin on myoVI's IQ domain with a red Qdot ($\lambda = 655$ nm) (Fig. 1*A*). Because myoV and myoVI travel to opposite ends of an actin filament, we determined the dominant motor within a myoV:myoVI complex by defining the barbed end of actin with gelsolin and an antigelsolin antibody-conjugated Qdot ($\lambda = 655$ nm) (Fig. 1 *A* and *B*, and Movies S1–S3). For each complex, run length and directional velocity were measured, where positive velocity indicated movement toward the barbed end of actin (i.e., dominated by myoV), whereas negative velocities indicated movement toward the pointed end (i.e., dominated by myoVI).

At a myoV:myoVI:Qdot-cargo conjugation ratio of 1:1:1, the velocity distribution for the 115 complexes analyzed was well described ($R^2 = 0.88$) by three distinct populations (Fig. 1*C*). The majority of these complexes (79%; 91/115) moved in the positive direction, confirming that myoV predominated, whereas only 21% (24/115) of these complexes were dominated by myoVI. For comparison, the velocity distributions for single myoV and single myoVI motors are plotted in Fig. 1*C*. Because the velocity (341 ± 69 nm/s, $N = 23$) for the less frequent population of myoV:myoVI complexes dominated by myoV equaled ($p > 0.05$) that of a single myoV motor (378 ± 82 nm/s, $N = 78$), it was possible that at the 1:1:1 myoV:myoVI:Qdot-cargo conjugation ratio, two myoV were bound to the Qdot cargo. We estimated

Author contributions: M.Y.A., G.G.K., K.M.T., H.L.S., and D.M.W. designed research; M.Y.A. performed research; D.S., K.M.T., and H.L.S. contributed new reagents/analytic tools; M.Y.A., G.G.K., and D.M.W. analyzed data; and M.Y.A., K.M.T., H.L.S., and D.M.W. wrote the paper.

The authors declare no conflict of interest.

*This Direct Submission article had a prearranged editor.

[1]To whom correspondence should be addressed. E-mail: david.warshaw@uvm.edu.

See Author Summary on page 13887.

This article contains supporting information online at www.pnas.org/lookup/suppl/doi:10.1073/pnas.1104298108/-/DCSupplemental.

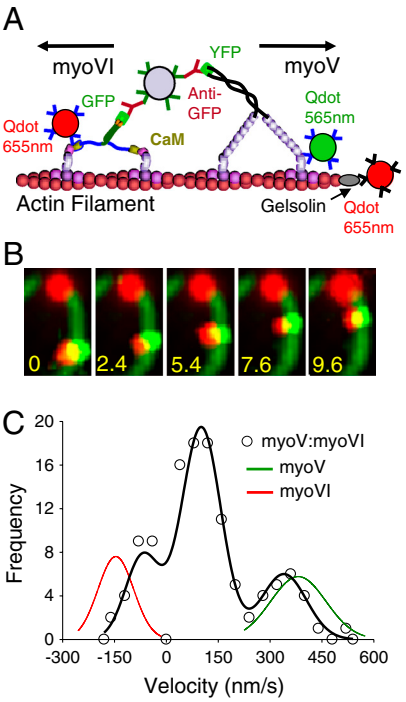

Fig. 1. MyoV:myoVI complex movement on actin filaments. (*A*) Illustration of experimental design drawn to scale. MyoV and myoVI were labeled with green and red streptavidin-functionalized Qdots, respectively, and linked together by a third anti-GFP antibody-coated Qdot (gray). The gelsolin-seeded actin filament was labeled at its barbed end using an antigelsolin antibody coupled to an anti-mouse IgG conjugated Qdot (red). (*B*) Sequential images of a myoV:myoVI complex (small red and green adjacent Qdots) moving on a polarity marked actin filament (green) toward the barbed end marked with red stationary Qdot (see *Materials and Methods*). The horizontal length of each image is 1.6 μm and time in seconds shown in the lower left corner. (*C*) Velocity distribution of myoV:myoVI complexes at 2 mM ATP (○). Positive velocities are indicative of travel toward barbed end. The histogram for complexes ($N = 115$) at myoV:myoVI:Qdot-cargo ratio of 1:1:1 was fitted to three Gaussian populations with mean ± SD velocities as follows (from left): -68 ± 50, 101 ± 57, and 341 ± 69 nm/s. As controls, the velocity distributions of myoVI (red) and myoV (green) alone are plotted with values of 146 ± 51 nm/s ($N = 76$) and 378 ± 82 nm/s ($N = 78$), respectively. For illustration purposes, these myoVI and myoV individual motor distributions are scaled to match the minor populations of the myoV:myoVI complexes.

this probability at 10% based on experiments that determined how many motors existed within a complex through Qdot fluorescence intensity measurements (see *SI Text* and Fig. S1*D*). To further characterize the impact of having multiple motors of one kind attached to the Qdot cargo, we determined the velocity distribution for a myoV:myoVI:Qdot-cargo conjugation ratio of 2:1:1, where the probability of having two myoV motors linked to a single myoVI was increased to 26% (Fig. S1*E*). This conjugation ratio resulted in 92% (i.e., 54/59) of the complexes being dominated by myoV (Fig. S2*B*), whereas at a 1:2:1 ratio, where the probability of having two myoVI motors linked to a single myoV was increased (Fig. S1*E*), 40% (i.e., 22/55) of the complexes were then dominated by myoVI (Fig. S2*C*). Therefore, conjugation ratios that resulted in complexes having two myoV or two myoVI led to dramatic shifts between the two populations at the opposite ends of the distributions (Fig. S2 *A–D*).

The largest population of complexes at the 1:1:1 ratio that was dominated by myoV moved 3.7-fold slower (101 ± 57 nm/s, $N = 68$; $p < 0.05$) than myoV alone and was the least affected by conjugation ratio (Fig. S2 *A–C*). These most likely represented a single myoV winning against a single myoVI. In contrast, for the 21% of total complexes dominated by myoVI at the 1:1:1 ratio (Fig. 1*C*), there was only one population with a velocity 2.2-fold slower (-68 ± 50 nm/s, $N = 23$; $p < 0.05$) than myoVI alone (-146 ± 51 nm/s, $N = 76$). Although a second population dominated by myoVI was not observed, half of these complexes were most likely associated with two myoVI attached to the Qdot cargo given the 10% probability for this scenario (see *SI Text* and Fig. S1).

The run length distributions for complexes that demonstrated slower velocities than that of a single motor were compared to single motors that traveled in the same direction (Fig. S3). For complexes that moved toward the pointed end (540 ± 90 nm, $N = 24$), there was no difference ($p > 0.05$) compared to the characteristic run length of a single myoVI motor (580 ± 90 nm, $N = 76$) (Fig. S3*A*). For complexes that moved toward the barbed end, the characteristic run length (625 ± 110 nm, $N = 68$) was reduced 1.8-fold ($p < 0.05$) compared to myoV alone ($1{,}120 \pm 103$ nm, $N = 78$) (Fig. S3*B*).

Coupled MyoV and MyoVI Motors Coordinate Their Stepping. With the motors individually Qdot-labeled, the stepping of each motor as it related to its coupled partner was determined. As controls, the step size and lifetimes for single myoV and single myoVI motors were characterized. As expected, when only one myoV head was labeled (20, 21), 72 ± 12 nm ($N = 139$) steps were observed (Fig. 2 *A* and *C*), which moved the motor's center of mass by half that amount—i.e., approximately 36 nm. No backward steps were detected. The lifetime of each myoV step was 87 ± 16 ms (Fig. 2*E*) (i.e., giving a 11.5 s^{-1} stepping rate). For myoVI alone, the forward step sizes were broadly distributed (-63 ± 20 nm, $N = 101$) with the appearance of occasional backsteps of 47 ± 15 nm ($N = 8$) (Fig. 2 *B* and *D*). This stepping pattern is believed to be a property of myoVI's inherent flexibility

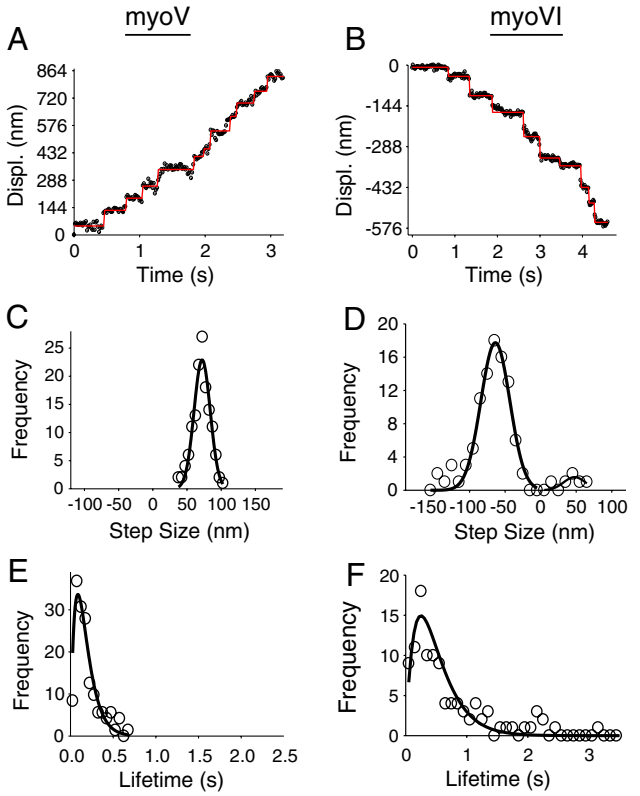

Fig. 2. Stepping characteristics of myoV and myoVI at 2 mM ATP. Displacement versus time traces of myoV (*A*) and myoVI (*B*) with steps identified by step finding routine in red. (*C*) Forward step-size distribution for single myoV (72 ± 12 nm, $N = 139$). (*D*) Forward and backward step sizes for a single myoVI [-63 ± 20 nm ($N = 101$), 47 ± 15 nm ($N = 8$), respectively]. (*E* and *F*) Step lifetime distributions of single myoV and myoVI (87 ± 16 ms, $N = 154$; 222 ± 24 ms, $N = 110$, respectively).

within the tail that allows the motor to take such long steps with short lever arms (22). The forward step lifetime of 222 ± 24 ms ($N = 110$) (Fig. 2*F*) resulted in a myoVI stepping rate of 4.5 s^{-1}.

For the 115 myoV:myoVI complexes that contributed to the velocity distribution at the 1:1:1 conjugation ratio (Fig. 1*C*), only 42 complexes exhibited clearly discernable steps from both motors simultaneously (Fig. 3*A*, *B*). Choosing these complexes eliminated those having a 2:1 ratio of motor types, where the spatial overlap of the point spread functions from two motors with the same color Qdot prevented steps from being detected (Fig. S2 *E* and *F*). For the 42 complexes analyzed, 34 were drawn from the predominant population that was dominated by myoV, which still took 70 ± 28 nm ($N = 177$) forward steps, although more broadly distributed and with 3.5-fold longer step lifetimes (303 ± 33 ms, $N = 190$) when compared to myoV alone (Fig. 3 *C* and *E*). In contrast to unloaded conditions where backsteps were rarely observed for a single myoV (14), 20% of the steps (43/220) taken by the dominant myoV motor were −63 ± 15 nm backsteps (Fig. 3 *A* and *C*). Interestingly, in the same complex, the linked myoVI motor walked continuously backward with 63 ± 37 nm ($N = 72$) steps and took occasional −58 ± 25 nm ($N = 18$) forward steps that coincided with myoV's backsteps (Fig. 3*A* and Fig. S4*C*).

A similar scenario was observed for the 8 out of 42 complexes for which myoVI dominated (Fig. 3*B*). In this case, myoVI took −57 ± 30 nm ($N = 82$) forward steps and 49 ± 30 ($N = 9$) backsteps, both of which were indistinguishable ($p > 0.05$) from the steps that a single myoVI took by itself (Figs. 2*D* and 3*D*). However, the forward step lifetimes (438 ± 43 ms, $N = 92$) were 2.0 times longer than myoVI alone (Figs. 2*F* and 3*F*). Once again, the losing motor, in this case myoV, took 68 ± 28 nm ($N = 74$) backward steps continuously (Fig. 3*B* and Fig. S4*A*). When the myoVI occasionally stepped backward during a run, myoV responded with a 66 ± 23 nm ($N = 11$) forward step (Fig. 3*B* and Fig. S4*A*).

Analysis of the spatial relationship and timing between steps of the opposing motors in the myoV:myoVI complex provided further insight to their mechanical interactions. Regardless of the dominant motor, the two motors either maintained a constant separation distance between Qdot labels (Fig. 4 *A* and *B*) or alternated between short and long separation distances (Fig. 4 *C* and *D*). To emphasize this spatial pattern, the interhead distance between Qdot labels for each step was determined and then the difference in this distance value between two consecutive steps calculated (i.e., pairwise difference). When analyzed in this manner, the histogram of pairwise differences when myoV dominated was best described by 3 Gaussians ($R^2 = 0.89$) (Fig. 4*E*) with a similar distribution ($R^2 = 0.90$) when myoVI dominated (Fig. 4*F*). The pairwise differences near 0 nm resulted from complexes where the two motors maintained a constant interhead distance within a run (Fig. 4 *A* and *B*), whereas the larger positive and negative pairwise differences reflected those complexes where the interhead separation alternated between steps (Fig. 4 *C* and *D*). In addition, for those complexes where the interhead distance remained constant within a run, the lead time or lag time between when the winning motor took its step relative to the losing motor was within 19 ± 53 ms ($N = 71$) (Fig. S5). Another measure of motor coordination was estimated by calculating the peak normalized cross-correlation between displacement versus time traces for the coupled myoV and myoVI motors. This quantity represents

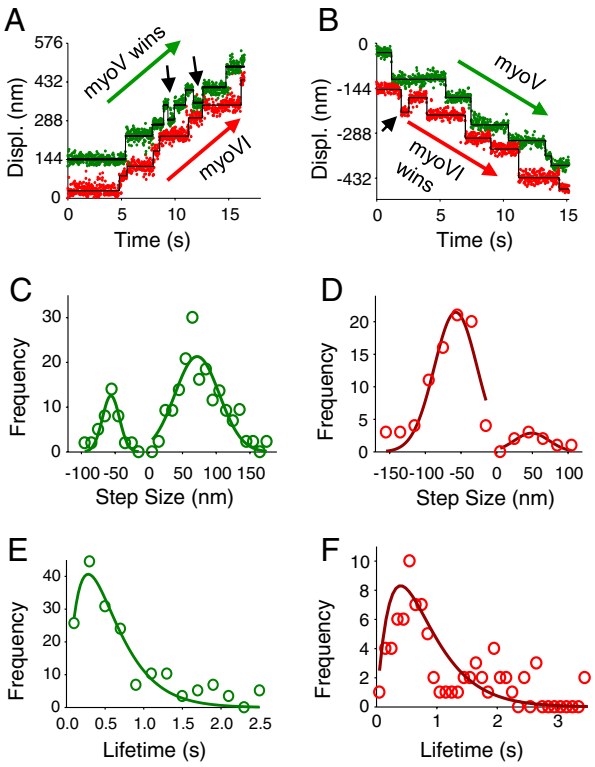

Fig. 3. Stepping characteristics of myoV:myoVI complex. (*A*) When myoV (green) dominates, it takes forward steps with occasional backsteps (black arrows). MyoVI (red) resists by taking backward steps. (*B*) When myoVI (red) wins and steps forward, the losing myoV motor (green) steps backward. (*C*) Step-size distribution of myoV when dominating within a complex, taking 70 ± 28 nm ($N = 177$) forward and fewer −63 ± 15 nm ($N = 43$) backward steps. (*D*) When myoVI wins, the forward and backward step sizes of myoVI are −57 ± 30 nm ($N = 82$) and 49 ± 30 nm ($N = 9$), respectively. (*E*) When myoV dominates, its step lifetime is 303 ± 33 ms ($N = 190$). (*F*) When myoVI dominates, its step lifetime is 438 ± 43 ms ($N = 92$).

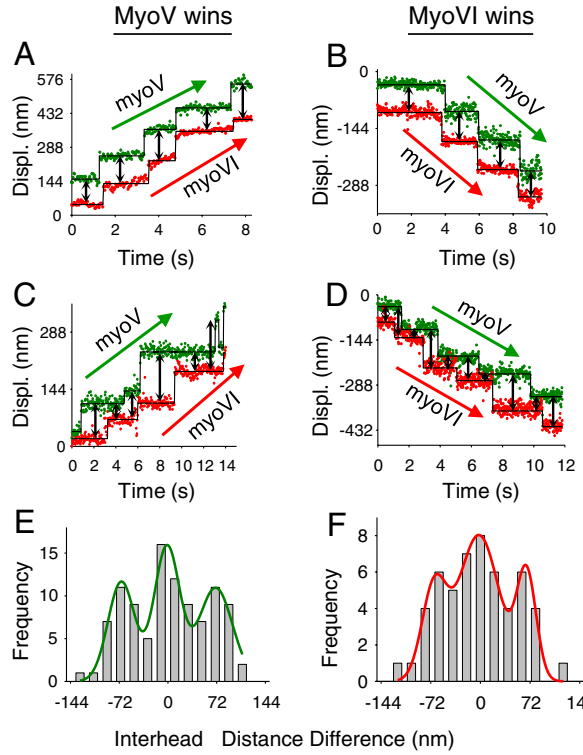

Fig. 4. Two stepping patterns of the myoV:myoVI complex. (*A* and *B*) Regardless of the dominant motor, the interhead distance between labeled heads (double-headed arrow) of myoV and myoVI remains constant. (*C* and *D*) Interhead distances alternate between short and long distances (double-headed arrow). (*E*) When myoV wins, the pairwise difference distance histogram (i.e., interhead distance differences between consecutive steps) shows three populations centered at −68 ± 20, 1 ± 19, and +70 ± 25 nm ($N = 101$). (*F*) When myoVI wins, the pairwise difference distance histogram also shows three populations centered at −67 ± 18, −2 ± 29, and +66 ± 14 nm ($N = 55$).

the similarity between two time dependent signals independent of phase, with a value of one indicating identical stepping. Nine traces with a total of 100 steps yielded an average peak cross-correlation of 0.98 ± 0.01.

Although the stepping dynamics of the two motors are highly coordinated in many cases, 13% of the original 115 complexes at the 1:1:1 conjugation ratio demonstrated more complicated stepping behaviors. For example, during a single step in Fig. S6*A*, the myoV head remained stationary while the myoVI head switched between two well-defined positions, a potential case where myoVI attempted to step forward, but was unable to, due to the resistance of the myoV motor. Another example was one in which the myoVI head appeared to be exploring space in a diffusional search (Fig. S6*B*) or to be dragging behind myoV (Fig. S6*C*).

Effects of ADP on Linked MyoV:MyoVI Transport. We explored the potential for changes in ADP concentration to shift the motor dominance to myoVI, based on the differential effects that elevated ADP has on myoV and myoVI processivity (23, 24) and the ability of myoVI to act as an anchor in the presence of ADP and resistive load (23). As controls, the percentage of stationary motors on actin, the velocities, and the run lengths for both myoV and myoVI were determined independently in the presence of varying ADP and 2-mM saturating ATP. As previously observed for myoV (24), both velocity and run length were reduced with increasing ADP ($p < 0.05$) (Fig. 5 *A* and *B*). In contrast, the myoVI run length (Fig. 5*B*) increased significantly at 50 μM ADP ($p < 0.05$) without any effect on velocity (Fig. 5*A*), similar to previous studies (25). Increasing ADP to 500 μM restored the myoVI run length to that seen in the absence of ADP ($p > 0.05$), although velocity decreased 1.92-fold (Fig. 5*A*). The enhanced or unchanged run length for myoVI in the presence of ADP, coupled to the reduction seen with myoV, may put myoVI at an advantage to dominate within a myoV:myoVI complex. Interestingly, with increasing ADP concentration, the percentage of stationary complexes on actin was greater than either motor by itself ($17.2 \pm 3.7\%$, total $N = 2{,}121$ at all ADP concentrations) and increased from 40% at 0 μM to 90% at 500 μM ADP (Fig. 5*E*). For the same ADP concentrations, the percentage of total complexes that were motile and dominated by myoV decreased from 44% at 0 μM to only 6% at 500 μM ADP (Fig. 5*E*). Upon closer inspection of these seemingly stationary complexes in the presence of ADP, myoVI maintained a fixed position on actin for extended periods of time, whereas myoV appeared to be in dynamic stall and took multiple forward and backward steps (Fig. 5*F*).

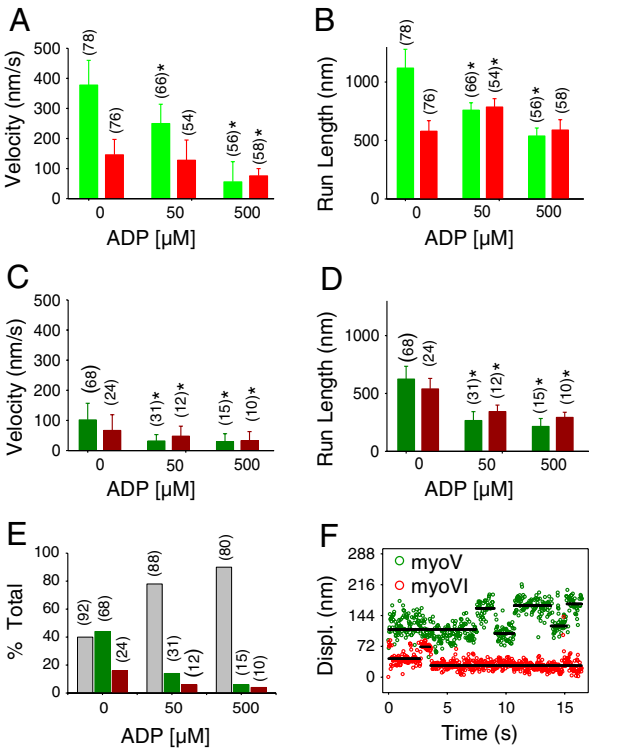

Fig. 5. ADP effects on the processive movement of myoV, myoVI, and myoV:myoVI complexes. For panels *A*–*D*, the number in parentheses is the number of runs. Asterisks indicate statistical significance in comparison to 0 μM ADP ($p < 0.05$). (*A*) Velocities of myoV (green) and myoVI (red) in the presence of 2 mM ATP and varying ADP as the mean ± SD. (*B*) Characteristic run lengths of myoV (green) and myoVI (red) in the presence of 2 mM ATP and varying ADP as the mean ± SE. (*C*) Velocities of myoV:myoVI complexes when myoV dominates (dark green) and when myoVI dominates (dark red) in the presence of 2 mM ATP and varying ADP as the mean ± SD. (*D*) Characteristic run lengths of myoV:myoVI complexes when myoV dominates (dark green) and when myoVI dominates (dark red) in the presence of 2 mM ATP and varying ADP as the mean ± SE. (*E*) Percentage of the total complexes interacting with actin that are stationary (gray), motile and dominated by myoV (dark green), and motile and dominated by myoVI (dark red) with the total number of complexes in parentheses in the presence of 2 mM ATP and varying ADP. (*F*) MyoVI acting as an anchor in presence of 2 mM ATP and 500 μM ADP. MyoVI (red) maintained a fixed position while myoV (green) appeared stalled while taking multiple forward and backward steps.

Discussion

We developed an in vitro model system that physically linked a single myoV and a single myoVI to a common cargo. As these two classes of motors attempted to carry the same cargo in opposite directions, we characterized the stepping dynamics of each motor to determine how mechanical interactions between motors resulted in myoV winning this tug of war most of the time and how changes in ADP concentration switched myoVI's role from transporter to anchor.

Why Does MyoV Dominate over MyoVI During Cargo Transport? A simple explanation for why myoV dominated 79% of the motile myoV:myoVI complexes is that myoV may generate higher stall forces. However, with similar stall forces (1.5–3 pN) for both myoV (14, 17, 26) and myoVI (16, 23, 27), other factors such as the resistive force that each motor imposes on its partner must be considered.

When myoV dominated, its forward step duration was prolonged 3.5-fold and it began taking backsteps 20% of the time (Fig. 3 *C* and *E*). In the absence of resistive load, myoV rarely (0.3% probability) takes a backstep (14), with none observed in this study. Therefore, knowing how resistive load (14) affects myoV's backstep probability (Fig. S7*A*) and myoV's forward step duration (Fig. S7*B*), we estimate that myoVI resists with 1.25–1.40 pN. By a similar analysis we estimate myoV's resistive load to myoVI as 2.0–2.1 pN (see Fig. S7*C*).

As the losing motor walks backward in presumably a hand-over-hand manner (20, 21, 28–30), the winning motor must generate sufficient force to detach the leading head of the losing motor, as well as reverse the powerstroke of the trailing head (Fig. 6). Ishiwata and coworkers (15) measured the unbinding force of single-headed S1 constructs of myoV (4.0 pN) and myoVI (2.6 pN) in the presence of 1 mM ADP. Assuming that the leading heads of both myoV and myoVI are strongly bound to actin with ADP in the active site (25, 31), the 1.54 greater force needed to unbind myoV is remarkably similar to the approximately 1.50 greater resistive loads we estimate above. With myoV and myoVI having similar stall forces, we propose that the motor requiring a higher unbinding force will resist being pulled backward to a greater extent, increasing its probability of dominating, which in this case is myoV. This prediction is in agreement with assumptions in a stochastic tug-of-war model developed by Muller et al. (12) in which the direction of cargo transport driven by two groups of opposing molecular motors is governed by the

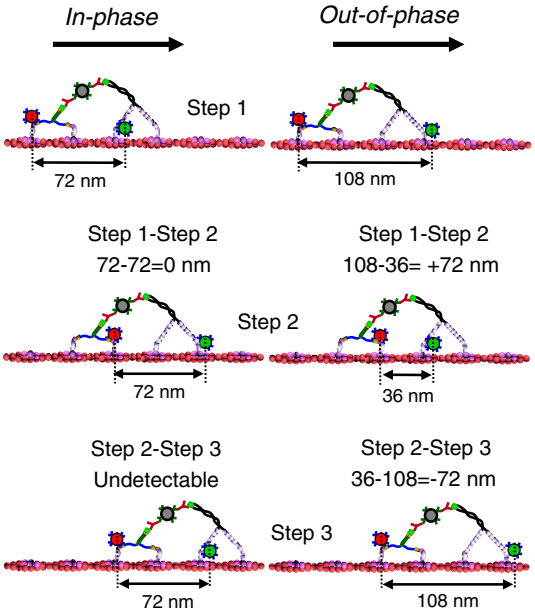

Fig. 6. Stepping patterns within a myoV:myoVI complex. A model of coordinated stepping patterns for three consecutive steps (e.g., when myoV wins the tug of war) classified into *In-Phase* and *Out-of-Phase* based on the position of the label for the two motors (see text for details). For in-phase stepping, the distance between the two labeled heads will always be same (i.e., 72 nm) in every processive step. However, for out-of-phase stepping, this distance will alternate between long and short distances (i.e., 108 and 36 nm).

comparative strength of the two motors; defined for each motor as $f = F_s/F_d$, where F_s is the stall force and F_d is the force required to detach the motor from its track. With F_s the same for the two motors, F_d becomes the only factor that distinguishes these two motors as we predicted above. Although our simple model is predictive, the data presented here could be the foundation for a more formal quantitative and mechanistic model that goes beyond the coordination of a single myoV linked to a single myoVI in order to explain cargo transport by a mixed population of the two motor types.

MyoVI dominated in 21% of the cases, but based on the discussion above it is not apparent why myoVIU would ever win. We can account for at least half of these due to the presence of two myoVI being bound to the cargo (see *SI Text* and Fig. S1). A potential scenario for the other half is that, although the illustration presented in Fig. 1*A* shows the two motors aligned along the top of the actin filament, it is possible that the motors travel along the lateral faces of the actin filament but on opposite sides, as recently observed for processive myoV by atomic force microscopy (32). If so, then the linkage between the two motors would straddle the actin filament, imposing an off-axis load to each motor. Ishiwata and coworkers (33) recently reported that, in response to certain angles of off-axis resistive loading, myoV took fewer processive steps, which they attribute to the off-axis sensitivity of the myoV unbinding force (i.e., F_d). Therefore, for the cases where myoVI dominated, potential off-axis resistive loading may have reduced myoV's F_d.

MyoV and MyoVI Coordinate Their Stepping. Analysis of the timing between steps (Fig. S5) and the stepping patterns (Fig. 4) of each motor in the complex suggest that the losing motor coordinates its backward stepping with the forward steps of the dominant motor. Fig. 6 is a to-scale illustration of the complex when myoV dominates, with two potential scenarios for motor labeling. With the actin filament adhered to the coverslip surface and due to the dimensions of the motors and Qdot, we propose that the number of actin-binding sites available to both motors should be limited so that motors are centered 72-nm apart. Secondly, given that the motor Qdot labeling is random, either the leading or the trailing head will be labeled (see Fig. 6). The stepping pattern associated with these two scenarios is classified as either "in-phase" or "out-of-phase." For the in-phase scenario, by appearance both motors have the same relative head labeled. Therefore, when myoV steps forward and myoVI follows by stepping backward, the distance between two labeled heads is always maintained at 72 nm (Fig. 6, *Left*). For the out-of-phase case, the motors are labeled on opposite heads so as the motors step coordinately, the distance between Qdots will alternate between 108 and 36 nm (Fig. 6, *Right*). Both situations were observed experimentally (Fig. 4 *A*–*D*). For these two scenarios, the pairwise difference in the interhead separation should always be approximately 0 nm for the in-phase case (Fig. 6, *Left*), while alternating between +72 and −72 nm for the out-of-phase case (Fig. 6, *Right*). Given that these values agree with the three populations defined by the pairwise difference histogram (Fig. 4 *E* and *F*), the positions of the two motors are spatially well defined, and the dominant motor forces the losing motor to step backward in a coordinated and a synchronous manner (see *Results*).

The coordinated stepping suggests that the myoV and myoVI motors must be physically coupled through a rigid linkage, otherwise the timing signals for step synchronization (Fig. S5) would not be communicated. Coordination could result from step changes in the linkage tension that may occur if the winning motor was to step first (i.e., link tension rises) versus the losing motor taking its backstep first (i.e., link tension falls). This scenario could explain why the winning motor's step is equally distributed between it leading and lagging the step of the losing motor (Fig. S5). Interestingly, the steady-state linkage tension and putative communication signals must have been maintained constant for the entire run because there was no evidence for a winning motor becoming a losing motor for more than one step. With greater motor numbers and with the physical properties of the cargo itself being dynamic, motor coordination and synchronization will be muted, leading to bidirectional transport within a run as observed for axonal transport (34) and modeled as shifts in the winning population of motors (13).

Implications for Regulating Cargo Transport in Vivo. The ability of one molecular motor to dominate its oppositely directed partner raises questions of how opposing motors attached to intracellular cargo are regulated to ensure proper cargo delivery. Regulation could involve modulating the processive properties of the individual motors or varying the number of motors of a given type. For example, previous studies suggest that myoVI in the presence of ADP and resistive load switches roles from cargo transporter to anchor (23). This shift to a prolonged strongly bound state is due to resistive load increasing myoVI's sensitivity for ADP while decreasing that for ATP (23). When the ADP concentration was increased in the presence of 2 mM ATP, the most dramatic effect in our assay was that the percentage of stationary myoV:myoVI complexes on actin increased (i.e., up to 90% at 500 μM ADP), which was not the case for the individual motors under identical conditions. When the individual motors within the complex were monitored under this condition, myoVI maintained its position while myoV was dynamically stalled stepping forward and backward (Fig. 5*F*). Thus, myoVI can effectively anchor the cargo in the presence of micromolar ADP concentrations that are physiological (19, 35–37), which implies that the differential effects of ADP on myoV and myoVI (see Fig. 5 *A* and *B*) could serve as an in vivo regulator that links myoVI function to the metabolic state of the cell (19).

Varying the number of a given motor type could be accomplished by regulating the active state of one motor type relative to the other (38). We varied the motor number in vitro by altering the myoV:myoVI:Qdot-cargo conjugation ratio, which shifted

whether myoV or myoVI was the dominant motor (Fig. S2 *A–C*). Such shifts in motor numbers may occur in vivo, for example, by local increases in calcium concentration in response to external stimuli, which would inhibit myoV processivity as observed in vitro (39, 40). In addition, the actin tracks on which the motors travel, through actin-binding proteins, could differentially impact different classes of myosin motors. As recently reported (41), the differential localization of tropomyosin in yeast can enhance the activity of two class V myosins (Myo51p and Myo52p) while inhibiting that of a class I myosin (Myo1p), providing a means for spatially regulating myosin function and cargo delivery. A similar mechanism has been proposed for regulating kinesin/dynein transport on microtubules via the presence of tau-protein binding to the microtubule (42). Modifiers that alter the number of engaged motors in effect would eliminate or bias (43–45) the inherent tug of war that would exist between opposing motors as observed in this study.

Future efforts to define the various regulatory mechanisms that govern intracellular transport will benefit from parallel in vitro single molecule biophysical and in vivo cell biological approaches. Building complexity in vitro should allow the impact of motor number and type, the size and physical properties of the cargo itself, and modifications to the tracks on which the motors travel, to be characterized. In addition, with intracellular fluorescent labeling and tracking of individual motors and cargo to which they are attached now possible (46), defining the dynamic roles that each motor plays and how these roles are regulated while sharing transport duties with partner motors should be within reach.

Materials and Methods

Protein Expression and Purification. A double-headed myoV heavy meromyosin construct was engineered by truncating the full length mouse heavy chain at residue 1098, followed by a YFP and a FLAG epitope tag at the C terminus to facilitate purification after expression in the *Baculovirus*/Sf9 cell system, as described previously (24, 47). The construct also contained an N-terminal biotin tag which consists of 87 amino acids residues (Met70-Glu156) from the *Escherichia coli* biotin carboxyl carrier protein, which is biotinated at a single lysine during expression in Sf9 cells (48). The biotin tag was used for attachment to streptavidin-conjugated Qdots (Invitrogen). The myoV construct was coexpressed with a calcium-insensitive calmodulin (CamΔall) as described previously (49).

For the double-headed myoVI construct, the porcine myoVI cDNA was truncated at Arg-994 (50), sequentially followed by an eGFP cDNA (Clontech), a leucine zipper (GCN4) to ensure dimerization, and then a FLAG tag at the C terminus to facilitate purification. This construct was expressed in Sf9 cells, as described previously (16, 51). The myoVI neck contains a single IQ motif, which binds an exchangeable calmodulin (CaM) (52, 53). Therefore a biotin-tagged CaM was expressed and exchanged onto the myoVI molecule for specific labeling with streptavidin-Qdots as described previously (30).

Buffer composition is as follows: Buffer A, 25 mM imidazole (pH 7.4), 4 mM $MgCl_2$, 1 mM EGTA, 50 mM KCl, 10 mM DTT; Buffer B, Buffer A plus 1 mg/mL BSA; Buffer C, 25 mM imidazole (pH 7.4), 4 mM $MgCl_2$, 1 mM EGTA, 300 mM KCl, 10 mM DTT; Buffer D, Buffer B plus 2 mM ATP.

Polarity Marked Actin Filaments. To determine actin filament polarity, actin polymerization was initiated off of gelsolin-actin fragments. These fragments were formed by mixing 10 μL of 1 μM gelsolin (Cytoskeleton, Inc.) and 10 μL of 2 μM monomeric globular (G) actin in G-actin buffer (2 mM Tris-Cl, 0.2 mM $CaCl_2$, 0.2 mM ATP, pH 7.6) and then incubated overnight at 4 °C. These fragments were labeled with Qdots that were conjugated to antigelsolin antibodies as follows: 2 μM mouse antigelsolin antibody (Sigma) was mixed with an equal volume of 1 μM goat $F(ab')_2$ anti-mouse IgG conjugated-Qdot (Invitrogen; emission 655 nm, red) in G-actin buffer and incubated for 1–2 h on ice. To label the fragments, equal volumes of gelsolin-actin fragments and antibody-coated Qdots were mixed and then incubated for 2 h on ice. The mixture was diluted fivefold in G-actin buffer to a final Qdot and actin concentrations of 0.1 and 0.2 μM, respectively. Then G actin was added to the mixture to a final actin concentration of 2.4 μM with actin filaments formed by adding KCl to a final concentration of 50 mM and incubating for an hour at room temperature, resulting in short actin filaments that were Qdot labeled at the gelsolin or barbed end of the filament. To create long actin filaments, at this point we added 3–5 μM filamentous actin that then annealed to the ends of the Qdot-labeled shorter filaments. These filaments were then labeled with TRITC-phalloidin (Invitrogen) at an equimolar phalloidin to actin ratio in Buffer A and incubated for an hour at room temperature and then stored at 4 °C.

MyoV:MyoVI Complex Formation. The myoV:myoVI complex consisted of individual myoV and myoVI motors that were labeled with different color Qdots and then were linked together through a third Qdot that served as a cargo (Fig. 1*A*). The individual motors were first Qdot labeled. For myoV, we mixed 4 μL of 1 μM streptavidin-Qdots from the commercial stock (Invitrogen: emission 565 nm; green) to 1 μL of 1 μM myoV in Buffer B. After 10 min of incubation on ice, we added biotin (Sigma) in Buffer A to a final concentration of 40 μM to block any unoccupied biotin-binding sites on the streptavidin-Qdot. MyoVI was labeled similarly but with a different color streptavidin-Qdot (Invitrogen; emission 655 nm; red). We used a third Qdot as a cargo to which the myoV and myoVI motors were attached via the C-terminal YFP on myoV and GFP on myoVI. Therefore, goat $F(ab')_2$ anti-mouse IgG conjugated-Qdots (Invitrogen; emission 800 nm, which are visibly silent in our imaging system) were initially conjugated to anti-GFP antibodies (Invitrogen; 3E6) at a Qdot:antibody molar ratio of 1:3.4 in Buffer A for 2–3 h on ice. Finally, the myoV:myoVI:Qdot-cargo complex was formed by mixing green Qdot-labeled myoV, red Qdot-labeled myoVI, and antibody-coated Qdot cargo at a 1:1:1 molar ratio and incubated 30 min on ice.

Motility Assay. The myoV:myoVI complex movement was observed in a 20-μL flowcell, constructed from glass coverslips and then placed on a microscope stage (see below). First, 20 μL of *N*-ethylmaleimide-modified myosin (54) at 0.5 mg/mL in Buffer C was introduced for 2 min to create the attachment strategy for actin filaments, followed by a Buffer A wash. Then 20 μL of 1 mg/mL BSA in Buffer B was incubated for 2 min, followed by a Buffer A wash. Then the polarity marked actin filaments in Buffer A were infused into the flowcell and incubated for 2 min, followed by a Buffer D wash. Then, the myoV:myoVI:Qdot-cargo complex was diluted in Buffer D (plus 0.1 mg/mL CaM) to a final myoV concentration of 0.2–0.5 nM and then infused into the flowcell.

Data Analysis. All motility experiments were performed at room temperature (23 ± 1 °C) using a through the objective Total Internal Reflection Fluorescence Nikon TE2000 inverted microscope (100×, PlanApo 1.49 n.a.) as described previously (55). Qdots and actin filaments were excited with an 488 nm argon laser. A dual view optical image splitter (Optical Insights) was used for simultaneous dual-color imaging. Typically, 1,000 images were captured at 15–60 frames/s with 2 × 2 pixel binning (1 pixel = 58.5 nm) using an intensified CCD camera (XR Mega-10Z running Piper control v2.3.14 software; Stanford Photonics). Image analysis was performed using Image J 1.41o (National Institutes of Health). Qdots were tracked using the SpotTracker 2D plugin to generate motion paths in two dimensions. The spatial resolution of the imaging system was 6 nm, determined by tracking a stationary Qdot on a glass surface over 500 frames as described previously (47). Digital images were corrected for color registration error by using a piezoelectric microscope slide holder (Nano-LP-100-USB203; Mad City Labs) to raster a 0.5-μm multicolored fluorescent microsphere (Ultra Rainbow Fluorescent Particles; Spherotech) throughout the visual field to map out the color registration error.

Run length and velocity were measured as described previously (56). In brief, run lengths were measured from the appearance of the complex until the run terminated. Run length distributions were fitted to $p(x) = Ae^{-x/\lambda}$, where λ is the characteristic run length constant, $p(x)$ is the relative frequency of the motor traveling a distance x, and A is a constant. The characteristic run length estimate is reported as mean ± SE of the parameter estimate of the fit. Velocity was calculated as the run length/run time with the velocity distribution fitted to a Gaussian: $y = A\exp\{-0.5[(x - x_0)/b]^2\}$, where x_0 is the mean velocity, b is the standard deviation, and A is a constant. All velocities are reported as the mean ± SD. Statistical significance was determined using the Kolmogorov–Smirnov test for run length comparisons (57) and the Student t test for velocity comparisons. Steps and their lifetimes were identified in displacement versus time traces by an unbiased, statistically based routine (58). The step-size distributions were fitted to a Gaussian as above and reported as mean ± SD. The step lifetime histograms were fit by $F(t) = tk^2e^{-kt}$ rather than a single exponential. Because the Qdot stepping data reported the position of only one head, the step lifetime was that of the labeled head combined with that of the unobserved step from the unlabeled head, which was assumed to have occurred at the same rate, k (21, 55). Step lifetimes are reported as $1/k$ as the mean ± SE of the parameter estimate of the fit.

ACKNOWLEDGMENTS. We thank members of the Warshaw Lab for helpful discussions, Samantha Previs for technical assistance, Shane Nelson for the microscope color correction map, Arthur Michalek for assistance with fluorescence intensity and cross-correlation analysis, Andrej Vilfan for his insightful comments, Monalisa Mukherjea for alternate myoVI constructs, and Elena Krementsova for expression of the myoV construct. This work was supported by National Institutes of Health Grants HL059408, GM094229 (to D.M.W.), DC009100 (to H.L.S.), GM078097 (to K.M.T.).

1. Buss FA, Kendrick-Jones J (2008) Myosin VI: A multifunctional motor. *Myosins A Superfamily of Molecular Motors*, Proteins and Cell Regulations, ed LM Coluccio (Spinger, Dordrecht, The Netherlands), Vol 7, pp 325–352.
2. Sellers J, Weisman S (2008) Myosin V. *Myosins A Superfamily of Molecular Motors*, Proteins and Cell Regulations, ed LM Coluccio (Springer, Dordrecht, The Netherlands), Vol 7, pp 289–323.
3. Gross SP, et al. (2002) Interactions and regulation of molecular motors in Xenopus melanophores. *J Cell Biol* 156:855–865.
4. Mallik R, Gross SP (2004) Molecular motors: Strategies to get along. *Curr Biol* 14: R971–982.
5. Welte MA (2004) Bidirectional transport along microtubules. *Curr Biol* 14:R525–537.
6. Patricio K, Karen Calabria L, Marco Peixoto P, Salmen Espindola F, Da Cruz-Landim C (2010) Characterization and localization of dynein and myosins V and VI in the ovaries of queen bees. *Cell Biol Int* 34:1041–1047.
7. Suter DM, Espindola FS, Lin CH, Forscher P, Mooseker MS (2000) Localization of unconventional myosins V and VI in neuronal growth cones. *J Neurobiol* 42:370–382.
8. Jamison DK, Driver JW, Rogers AR, Constantinou PE, Diehl MR (2010) Two kinesins transport cargo primarily via the action of one motor: Implications for intracellular transport. *Biophys J* 99:2967–2977.
9. Kunwar A, Vershinin M, Xu J, Gross SP (2008) Stepping, strain gating, and an unexpected force-velocity curve for multiple-motor-based transport. *Curr Biol* 18:1173–1183.
10. Leduc C, Ruhnow F, Howard J, Diez S (2007) Detection of fractional steps in cargo movement by the collective operation of kinesin-1 motors. *Proc Natl Acad Sci USA* 104:10847–10852.
11. Rogers AR, Driver JW, Constantinou PE, Kenneth Jamison D, Diehl MR (2009) Negative interference dominates collective transport of kinesin motors in the absence of load. *Phys Chem Chem Phys* 11:4882–4889.
12. Muller MJ, Klumpp S, Lipowsky R (2008) Tug-of-war as a cooperative mechanism for bidirectional cargo transport by molecular motors. *Proc Natl Acad Sci USA* 105:4609–4614.
13. Muller MJ, Klumpp S, Lipowsky R (2010) Bidirectional transport by molecular motors: Enhanced processivity and response to external forces. *Biophys J* 98:2610–2618.
14. Kad NM, Trybus KM, Warshaw DM (2008) Load and Pi control flux through the branched kinetic cycle of myosin V. *J Biol Chem* 283:17477–17484.
15. Oguchi Y, et al. (2008) Load-dependent ADP binding to myosins V and VI: Implications for subunit coordination and function. *Proc Natl Acad Sci USA* 105:7714–7719.
16. Rock RS, et al. (2001) Myosin VI is a processive motor with a large step size. *Proc Natl Acad Sci USA* 98:13655–13659.
17. Uemura S, Higuchi H, Olivares AO, De La Cruz EM, Ishiwata S (2004) Mechanochemical coupling of two substeps in a single myosin V motor. *Nat Struct Mol Biol* 11:877–883.
18. Clemen AE, et al. (2005) Force-dependent stepping kinetics of myosin-V. *Biophys J* 88:4402–4410.
19. Mora B, Narasimhan PT, Ross BD, Allman J, Barker PB (1991) 31P saturation transfer and phosphocreatine imaging in the monkey brain. *Proc Natl Acad Sci USA* 88:8372–8376.
20. Warshaw DM, et al. (2005) Differential labeling of myosin V heads with quantum dots allows direct visualization of hand-over-hand processivity. *Biophys J* 88:L30–32.
21. Yildiz A, et al. (2003) Myosin V walks hand-over-hand: Single fluorophore imaging with 1.5-nm localization. *Science* 300:2061–2065.
22. Mukherjea M, et al. (2009) Myosin VI dimerization triggers an unfolding of a three-helix bundle in order to extend its reach. *Mol Cell* 35:305–315.
23. Altman D, Sweeney HL, Spudich JA (2004) The mechanism of myosin VI translocation and its load-induced anchoring. *Cell* 116:737–749.
24. Baker JE, et al. (2004) Myosin V processivity: Multiple kinetic pathways for head-to-head coordination. *Proc Natl Acad Sci USA* 101:5542–5546.
25. Sweeney HL, et al. (2007) How myosin VI coordinates its heads during processive movement. *EMBO J* 26:2682–2692.
26. Mehta AD, et al. (1999) Myosin-V is a processive actin-based motor. *Nature* 400:590–593.
27. Nishikawa S, et al. (2002) Class VI myosin moves processively along actin filaments backward with large steps. *Biochem Biophys Res Commun* 290:311–317.
28. Lu H, Kennedy GG, Warshaw DM, Trybus KM (2010) Simultaneous observation of tail and head movements of myosin V during processive motion. *J Biol Chem* 285:42068–42074.
29. Okten Z, Churchman LS, Rock RS, Spudich JA (2004) Myosin VI walks hand-over-hand along actin. *Nat Struct Mol Biol* 11:884–887.
30. Yildiz A, et al. (2004) Myosin VI steps via a hand-over-hand mechanism with its lever arm undergoing fluctuations when attached to actin. *J Biol Chem* 279:37223–37226.
31. Rief M, et al. (2000) Myosin-V stepping kinetics: A molecular model for processivity. *Proc Natl Acad Sci USA* 97:9482–9486.
32. Kodera N, Yamamoto D, Ishikawa R, Ando T (2010) Video imaging of walking myosin V by high-speed atomic force microscopy. *Nature* 468:72–76.
33. Oguchi Y, et al. (2010) Robust processivity of myosin V under off-axis loads. *Nat Chem Biol* 6:300–305.
34. Hendricks AG, et al. (2010) Motor coordination via a tug-of-war mechanism drives bidirectional vesicle transport. *Curr Biol* 20:697–702.
35. Brosnan MJ, Chen L, Van Dyke TA, Koretsky AP (1990) Free ADP levels in transgenic mouse liver expressing creatine kinase. Effects of enzyme activity, phosphagen type, and substrate concentration. *J Biol Chem* 265:20849–20855.
36. Koretsky AP, Brosnan MJ, Chen LH, Chen JD, Van Dyke T (1990) NMR detection of creatine kinase expressed in liver of transgenic mice: Determination of free ADP levels. *Proc Natl Acad Sci USA* 87:3112–3116.
37. Williams SP, Fulton AM, Brindle KM (1993) Estimation of the intracellular free ADP concentration by 19F NMR studies of fluorine-labeled yeast phosphoglycerate kinase in vivo. *Biochemistry* 32:4895–4902.
38. Schroeder HW, 3rd, Mitchell C, Shuman H, Holzbaur EL, Goldman YE (2010) Motor number controls cargo switching at actin-microtubule intersections. *Curr Biol* 20:687–696.
39. Lu H, Krementsova EB, Trybus KM (2006) Regulation of myosin V processivity by calcium at the single molecule level. *J Biol Chem* 281:31987–31994.
40. Nguyen H, Higuchi H (2005) Motility of myosin V regulated by the dissociation of single calmodulin. *Nat Struct Mol Biol* 12:127–132.
41. Clayton JE, Sammons MR, Stark BC, Hodges AR, Lord M (2010) Differential regulation of unconventional fission yeast myosins via the actin track. *Curr Biol* 20:1423–1431.
42. Dixit R, Ross JL, Goldman YE, Holzbaur EL (2008) Differential regulation of dynein and kinesin motor proteins by tau. *Science* 319:1086–1089.
43. Ally S, Larson AG, Barlan K, Rice SE, Gelfand VI (2009) Opposite-polarity motors activate one another to trigger cargo transport in live cells. *J Cell Biol* 187:1071–1082.
44. Gross SP, Welte MA, Block SM, Wieschaus EF (2002) Coordination of opposite-polarity microtubule motors. *J Cell Biol* 156:715–724.
45. Laib JA, Marin JA, Bloodgood RA, Guilford WH (2009) The reciprocal coordination and mechanics of molecular motors in living cells. *Proc Natl Acad Sci USA* 106:3190–3195.
46. Watanabe TM, Higuchi H (2007) Stepwise movements in vesicle transport of HER2 by motor proteins in living cells. *Biophys J* 92:4109–4120.
47. Ali MY, et al. (2007) Myosin Va maneuvers through actin intersections and diffuses along microtubules. *Proc Natl Acad Sci USA* 104:4332–4336.
48. Cronan JE, Jr (1990) Biotination of proteins in vivo. A post-translational modification to label, purify, and study proteins. *J Biol Chem* 265:10327–10333.
49. Krementsov DN, Krementsova EB, Trybus KM (2004) Myosin V: Regulation by calcium, calmodulin, and the tail domain. *J Cell Biol* 164:877–886.
50. Park H, et al. (2007) The unique insert at the end of the myosin VI motor is the sole determinant of directionality. *Proc Natl Acad Sci USA* 104:778–783.
51. De La Cruz EM, Ostap EM, Sweeney HL (2001) Kinetic mechanism and regulation of myosin VI. *J Biol Chem* 276:32373–32381.
52. Bahloul A, et al. (2004) The unique insert in myosin VI is a structural calcium-calmodulin binding site. *Proc Natl Acad Sci USA* 101:4787–4792.
53. Menetrey J, et al. (2005) The structure of the myosin VI motor reveals the mechanism of directionality reversal. *Nature* 435:779–785.
54. Warshaw DM, Desrosiers JM, Work SS, Trybus KM (1990) Smooth muscle myosin cross-bridge interactions modulate actin filament sliding velocity in vitro. *J Cell Biol* 111:453–463.
55. Nelson SR, Ali MY, Trybus KM, Warshaw DM (2009) Random walk of processive, quantum dot-labeled myosin Va molecules within the actin cortex of COS-7 cells. *Biophys J* 97:509–518.
56. Ali MY, Lu H, Bookwalter CS, Warshaw DM, Trybus KM (2008) Myosin V and Kinesin act as tethers to enhance each others' processivity. *Proc Natl Acad Sci USA* 105:4691–4696.
57. Press WH, Teukolsky SA, Vetterling WT, Flannery BP (1992) *Numerical Recipes in C: The Art of Scientific Computing* (Cambridge Univ Press, Cambridge, UK), pp 623–626.
58. Kerssemakers JW, et al. (2006) Assembly dynamics of microtubules at molecular resolution. *Nature* 442:709–712.